Journal of Magnetic Resonance **140,** 325–339 (1999)
Article ID jmre.1999.1832, available online at http://www.idealibrary.com on IDEAL®

Fast Optimization of a Biplanar Gradient Coil Set

D. Tomasi,* E. C. Caparelli,* H. Panepucci,† and B. Foerster†

*Escuela de Ciencia y Tecnologia, Universidad Nacional de General San Martin, Alem 3901, 1651 San Andres, Buenos Aires, Argentina; and
†Departamento de Física e Informática, Instituto de Física de São Carlos, Universidade de São Paulo,
Av. Dr. Carlos Botelho 1465, CEP 13560-250 São Carlos, SP, Brazil

Received October 14, 1998; revised May 5, 1999

This work presents an approach for fast optimization of gradient coils, using the simulated annealing method. The shielding condition derived from a target field method and the analytical evaluation of the fields produced by simple geometries were used to reduce the computing time. This method is applied to the optimization of a shielded biplanar gradient coil set. Efficiency, inductance, and homogeneity of the gradient fields produced by the optimized geometries were studied as a function of the number of wires, for the longitudinal and transverse gradient coils. A prototype of the gradient set was made to test the proposed design method. The resulting experimental values of coil efficiency, inductance, field linearity, and shielding performance exhibit good agreement between theory and experiment.

INTRODUCTION

A great deal of effort has been made during the past years in magnetic resonance imaging (MRI) to develop coils producing uniform magnetic gradient fields with high efficiency and low inductance (*1*, *2*).

Coils producing uniform gradient fields for axial magnets were obtained using the target field (TF) approach and minimum inductance methods proposed by Turner and colleagues (*3–6*). In these works the desired magnetic fields are specified on cylindrical surfaces, and the current density is found in the reciprocal space linked to the coordinate space through the Fourier transform. The TF method also provides a shielding condition, which is frequently used to develop self-shielded gradient coils. Because this method usually results in coils with a large length-to-diameter ratio (LDR $\sim$ 4), constraints representing regions where the current density is set to zero are used to allow truncation of coils, resulting in a loss of gradient uniformity (*7*).

The TF method for planar geometries, first introduced by Yoda (*8*), was applied to design gradient coils with minimum inductance for axial magnets (*10*, *11*), but due to limitations on coil size the uniformity region is restricted.

In a recent work we presented an extension of Yoda's approach, to design a set of shielded biplanar gradient coils, to be used in electromagnet MRI systems (*12*). In that work we used simple geometries for the current densities optimized up to fifth-order terms in the magnetic field expansion.

Recently another method, called simulated annealing (SA), has been successfully employed for developing longitudinal and transverse gradient coils with cylindrical (*13–16*) and planar (*17*) geometries of restricted length. This method, introduced by Metropolis *et al.* (*18*), was applied to a great diversity of problems where the arrangement of elements in a large scale can be done by simulating the way in which a metal slowly cools to a minimum energy state. Unlike the TF method, discretization and restricted length are naturally taken into account in the SA method. The SA computing time depends strongly on the number of degrees of freedom of the annealing problem; typically several hours are required to achieve convergence (*13*).

In this work we show that the shielding condition derived from TF methods and the analytical evaluation of the fields produced by simple geometries, like circles and lines, can be used to develop rapidly converging SA routines.

METHOD AND NUMERICAL RESULTS

In the simulated annealing method for gradient coil design, the coil geometry is adjusted step by step through a set of random parameters. For this, a dimensionless error function, E, that may contain contributions from uniformity, efficiency, inductance, etc., is considered,

$$E = \sum_{i}^{N} \alpha(\langle G\rangle - G_i)^2 + \frac{\beta}{\langle G\rangle} + \gamma L + \cdots, \qquad [1]$$

where α, β, and γ are weighting factors for uniformity, efficiency, and inductance, respectively. N is the number of points in the evaluation region (ER) where the gradient field is calculated, L is the coil inductance, and $\langle G\rangle$ is the average value of the gradient in the ER, frequently evaluated from direct integration of the Biot–Savart law (*13*). To perform the minimization process the resulting error function at any step, E_i, is compared with that corresponding to the best previous configuration, E_0, by using the Boltzmann probability $P_i \sim \exp(-\Delta E/kT_i)$. Here, k is the Boltzmann constant, T_i the

1090-7807/99 $30.00

temperature of the system in thermal equilibrium, and $\Delta E = E_i - E_0$. Arrangements with $\Delta E < 0$ are always accepted while arrangements with $\Delta E > 0$ are accepted with probability P_i, which depends on T_i at step i (*13–16*).

After M rearrangements at fixed temperature the allowed excursions of free parameters are reduced and the annealing schedule is repeated S times until the local minimum of the error function is reached.

To optimize shielded gradient coils, the standard SA procedure uses n free parameters to model the primary coil and another m free parameters for the shielding coil (*13*), which are randomly varied. At each annealing step the gradient homogeneity and coil efficiency are calculated inside the primary coil, and the shielding performance is evaluated outside the shielding coil in order to optimize the wire arrangement using the annealing procedure described above. In this work we are proposing a fast simulated annealing method where the shielding current distribution is analytically derived and simple geometries for wires are employed, allowing the use of analytic expressions to calculate the gradient field inside the primary coil. This procedure, schematically compared with the standard procedure in Fig. 1, does not increase the necessary number of degrees of freedom in the annealing problem and quickly converges to the local minimum of E, resulting in a significant reduction of the computing time.

As we have shown before (*12*), a set of shielded biplanar gradient coils can be achieved considering a set of four planes perpendicular to the z axis where the shielding planes and the primary planes are placed at $z = \pm d$ and $z = \pm a$ ($d > a$), respectively. In the next two sections we detail the simulated annealing scheme used to optimize the longitudinal and the transverse gradient coils. It must be noticed that just as in the standard SA method we did not include the minimization of coil inductance in the annealing algorithm in order to reduce the computing time.

Longitudinal

The axial gradient coil has been modeled using n circular wires with radius R_i, $i = 1, \ldots, n$, placed in each primary plane. The wire distribution in the two primary planes must be identical to maximize the field uniformity, but the currents in each plane have to be opposite to produce an axial gradient.

Several authors (*13–16*) have obtained SA-optimized shielded coils adding m extra degrees of freedom into the annealing algorithm, to null the magnetic field outside the shielding coil. This increases the computing time for each annealing step and also the number of steps needed to reach the local minimum of E.

To reduce the CPU time, necessary to encounter this local minimum, we reduced the problem's degree of freedom to n in the following way: To obtain the shielding coil we used the shielding density, $j^d(r)$, derived from the planar TF method, which for $n = 1$ is related to the primary current by (*12*)

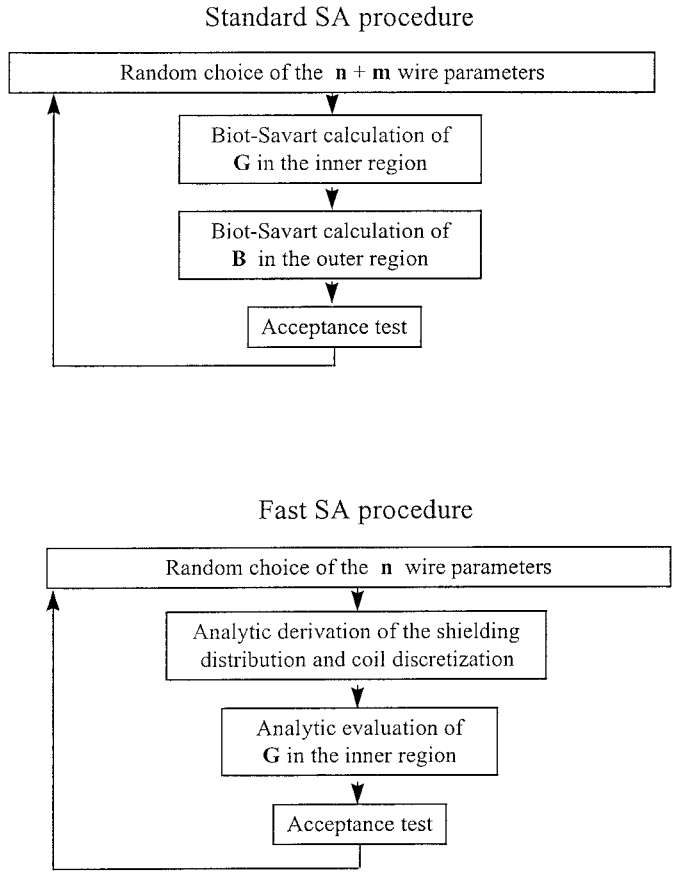

FIG. 1. Fast simulated annealing scheme compared with the standard one.

$$j^d(r) = -IR \int_0^\infty \xi \frac{\sinh(a\xi)}{\sinh(d\xi)} J_1(R\xi) J_1(r\xi) d\xi, \qquad [2]$$

where r is the axial distance, $J_1(x)$ is the Bessel function of order 1, and R is the radius of the wire carrying a current I. This relation between currents flowing in the primary and the shielding planes can be used to obtain, by superposition, the current density to shield a coil consisting of a set of circular wires of radius $\{R_i\}$. To approximate the continuous current density by a discrete wire arrangement, we choose a set of circular wires of radius $\{R_k\}$ calculated from

$$(k - 0.5) I_s = \int_0^{R_k} j^d(r) dr, \qquad [3]$$

where I_s is the current carried by the shielding wires.

Another strategy followed to reduce the CPU time was to look for regions where the gradient fields could be analytically evaluated. Unfortunately this methodology cannot always be used, but for the proposed geometry the gradient field can be expressed analytically along the z axis. The z component of the gradient field due to the k wire is

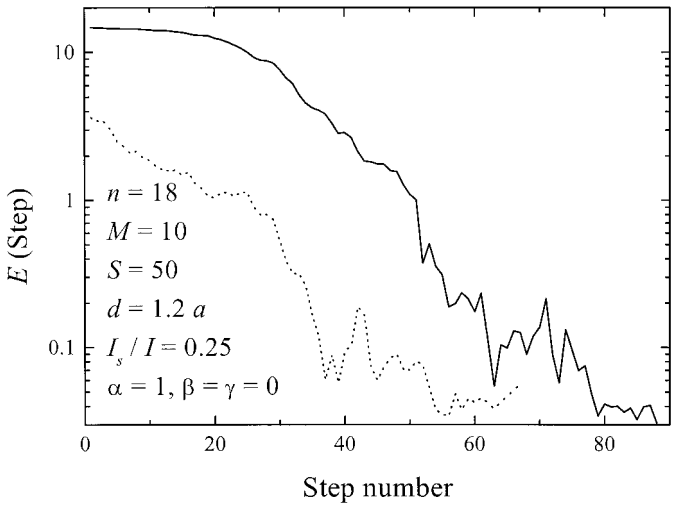

FIG. 2. Error function evolution of the simulated annealing procedure for the longitudinal gradient coil. Two different evolution curves are shown corresponding to two initial conditions for the wire distribution (see the text).

$$G_z^k(z) = \frac{3\mu_0 I}{2} \frac{R_k^2(z - z_k)}{[(z - z_k)^2 + R_k^2]^{5/2}}, \qquad [4]$$

where z_k is the z coordinate of the k wire.

We wrote a C code that computes Eqs. [1] to [4] to perform the annealing of a set of n wires on each primary plane.

The curves in Fig. 2 represent the evolution of the calculated error function, for accepted wire arrangements. Two different initial radius sets $\{R_i\}$ have been used showing that final configurations do not depend on the initial conditions. The solid curve corresponds to the initial set A, where all turns have the same radius, given by the Maxwell condition, which is $\{R_i = 1.154a\}$ for $i = 1, \ldots, n$, and the dotted curve corresponds to the initial set B where the n turns were distributed in two different groups having radius $\{R_i = a\}$ for $i = 1, \ldots, n/2$ and $\{R_i = 1.5a\}$ for $i = n/2 + 1, \ldots, n$. In both cases we set

- $n = 18$: number of wires in each primary plane;
- $d/a = 1.2$: ratio between the z coordinates of the shielding and primary planes;
- $\alpha = 1$, $\beta = 0$, $\gamma = 0$: for optimization of gradient homogeneity only;
- $M = 10$: number of rearrangements at fixed temperature;
- $S = 50$: number of temperature steps in the cooling scheme; the temperature at the i step is given by $T_{i+1} = T_0(1 - i/S)$, where T_0 is the initial temperature of annealing;
- $\Delta R = 0.1\, T_i/T_0$: the amplitude for random excursions of $\{R_i\}$ is a linear function of temperature;
- $kT = 50$: the initial temperature T_0 was chosen to accept larger excursions of radius $\{R_i\}$;
- ER $= (0, 0, z)$ with $0 \le z \le 0.75a$: the gradient fields were evaluated at 10 axial positions $z_i = i\, 0.075a$, to compute Eq. [1].

As shown in Fig. 2, the optimization procedure produces a significant reduction of the error function, which for the final configurations essentially does not depend on the initial set $\{R_i\}$. Furthermore, due to the probabilistic nature of the test used to accept or reject a given configuration, the algorithm can deal with relative minima without getting trapped.

Figure 3 shows the optimized set A corresponding to the primary coil of the axial gradient. This figure also shows the current density necessary to shield this final wire distribution as a function of the normalized radius r/a. To obtain a discrete distribution of this density we used 58 circular wires carrying a current $I_s = I/4$.

The improvement obtained in gradient homogeneity with the above procedure is shown in Fig. 4, where $2a \times 2a$ contour maps of the G_z fields are given in the (r, z) plane. In this figure the 5% contours correspond to black–white transition edges. A linear gray scale was introduced to increase resolution. Large continuous areas of the same gray level, in the center of Figs. 4C and 4D, indicate good gradient linearity. The gray-scale maps of Fig. 4 demonstrate the success of the optimization process in increasing the region of uniform gradient. This allows for a sufficiently large field of view (FOV) along the z axis without increasing the magnet gap.

Making $a = 25$ cm, the resulting coil has a diameter of 100 cm with a gap of 50 cm, usable for patient access despite some space taken by the RF coil. The coil would produce a gradient field of 6.6 mG/cm/A with a residual magnetic field at $z = \pm 37$ cm which is only 5% of the one which would be produced by the same coil without shielding. This means that the shielding is 95% effective. The coil inductance was numerically evaluated using (see the Appendix)

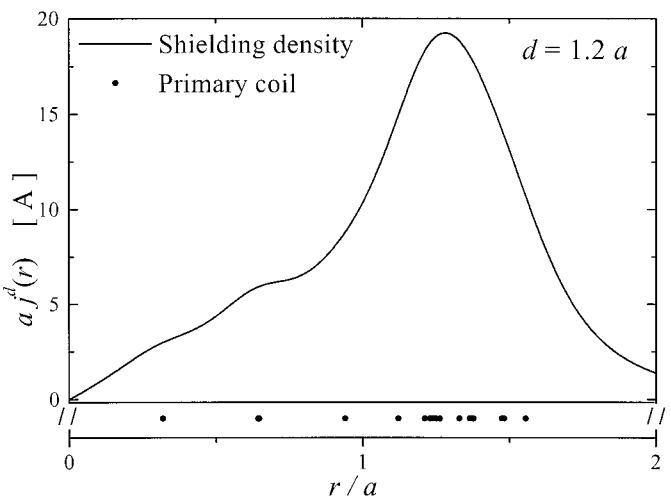

FIG. 3. Primary coil and shielding density for the optimized longitudinal gradient coil.

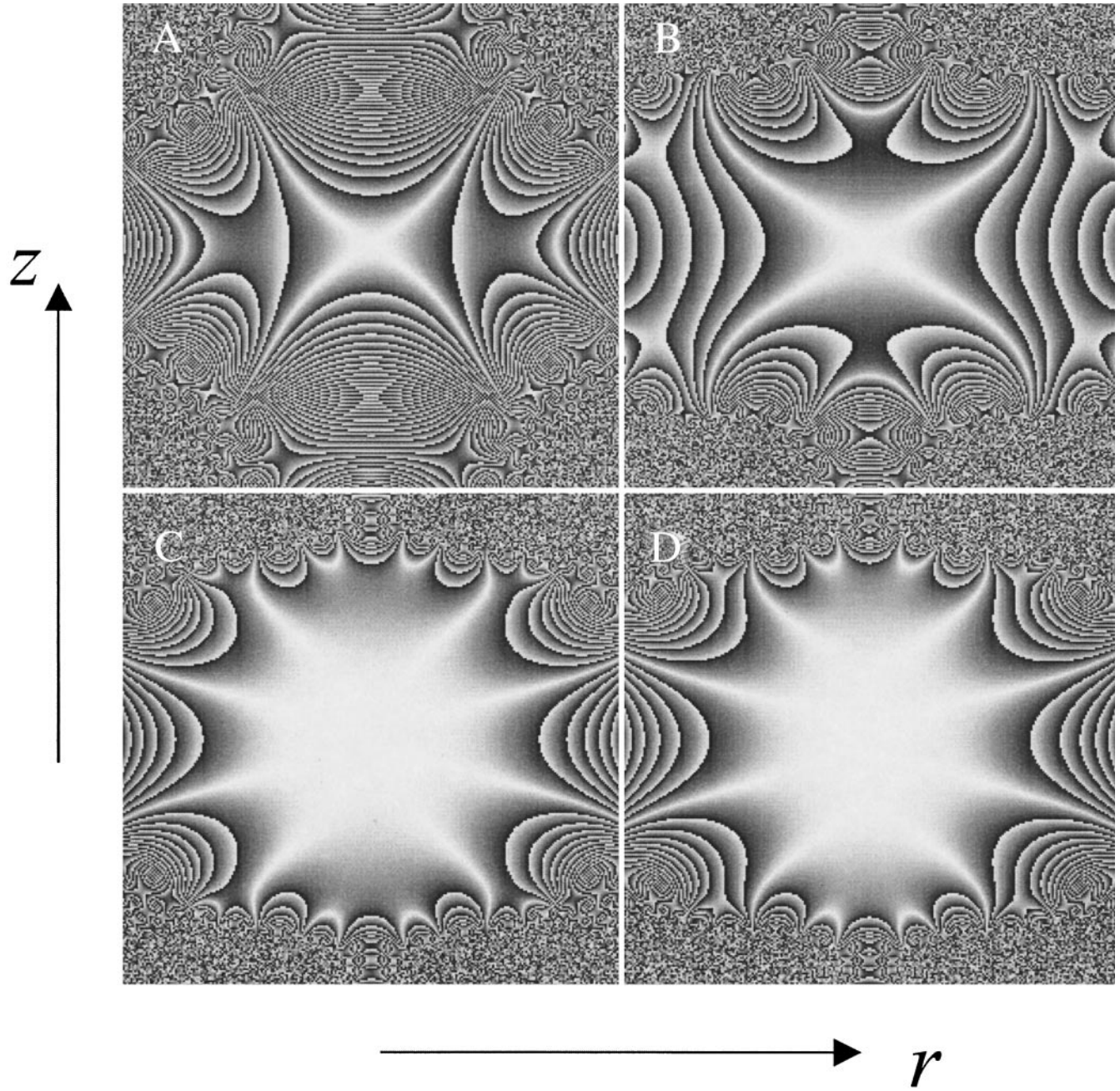

FIG. 4. $2a \times 2a\ G_z(r, z)$ maps produced by the longitudinal gradient coils as described in the text. (A) and (B) correspond to the initial configurations A and B. (C) and (D) correspond to the optimized configurations. A linear gray scale was used between the 5% contours, defined by the black–white transitions.

$$L = 4\pi\mu_0 \int_0^\infty \Big|\sum_{i=1}^{n} R_i J_1(R_i\xi)\Big|^2 \times \left(1 - \frac{\sinh(a\xi)}{\sinh(d\xi)}\, e^{-(d-a)\xi}\right) \sinh(a\xi) e^{-a\xi} d\xi, \qquad [5]$$

which includes self- and mutual inductances between the wires in the primary and shielding planes and resulted in $L = 280\ \mu$H.

To study the effects of the number of turns on the coil performance we evaluated the gradient field per unit current, η, at the magnet isocenter, and the coil inductance, using Eqs. [4] and [5], respectively, as a function of the number of wires n. Additionally, for each optimized configuration we have calculated the gradient field homogeneity in the ER using the quantity

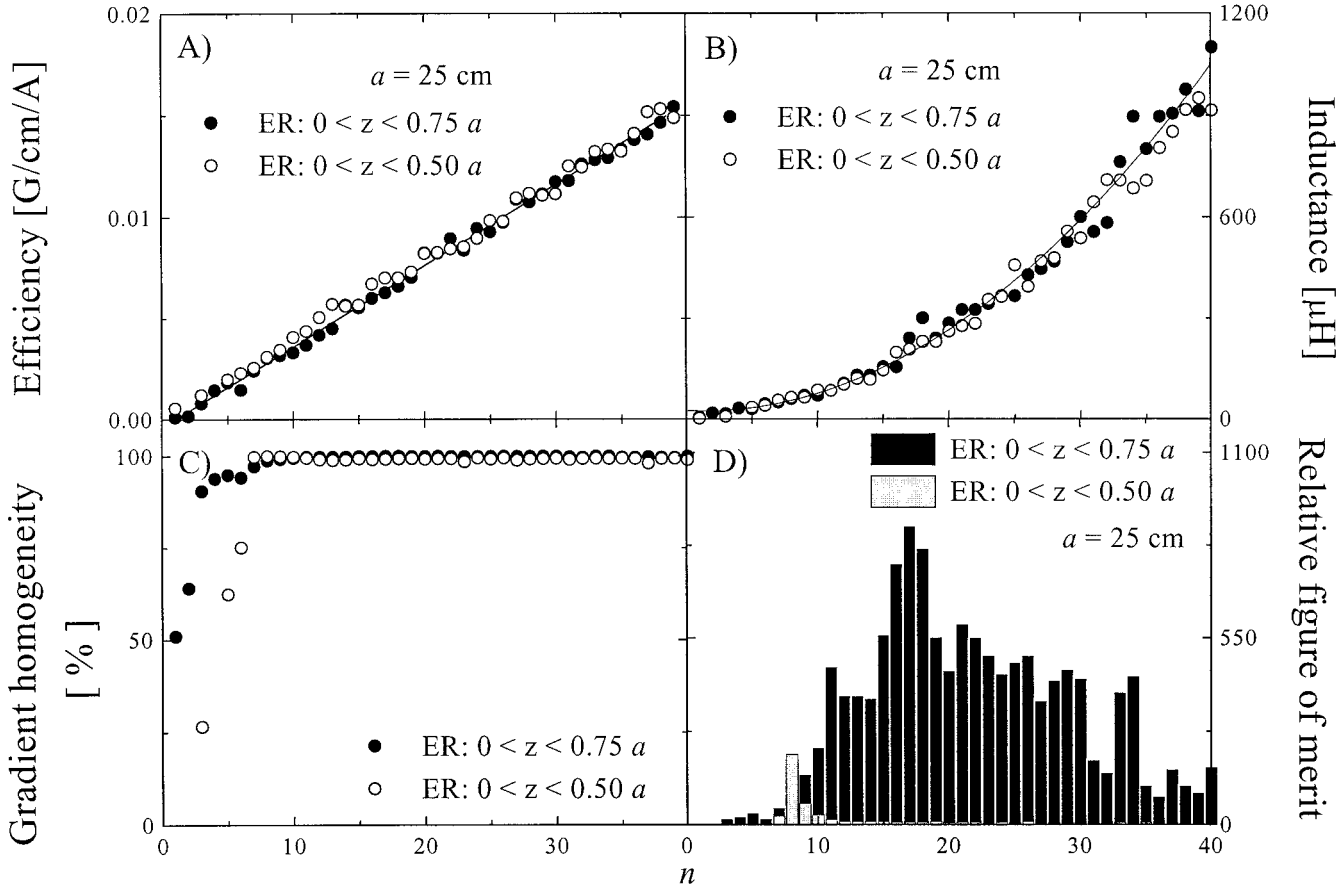

FIG. 5. Main characteristics of the optimized longitudinal gradient coils as a function of n for two different ER.

$$\sigma = \sqrt{\frac{1}{N}\sum_{i=1}^{N}\left(1 - \frac{G_z(z_i)}{\langle G_z\rangle}\right)^2}, \qquad [6]$$

where the gradient homogeneity is defined by $1 - \sigma$. To study the effects of the ER in the annealing process, we performed two kind of fast SA optimizations, evaluating Eq. [1] in two different ER intervals, ($0 \le z \le 0.75a$) and ($0 \le z \le 0.50a$), and keeping the other annealing parameters as above.

The results of this calculation are shown in Figs. 5A–5C. As we can see from Figs. 5A and 5B, η increases linearly with n, and L shows a parabolic growth.

The gradient homogeneity $1 - \sigma$, shown in Fig. 5C, presents a sharp increase at low n. In this region it depends on the ER, reaching 100% homogeneity at $n = 8$ for $0 \le z \le 0.50a$, and $n = 16$ for $0 \le z \le 0.75a$ which corresponds to a larger FOV.

The overall performance of the coil can be described by the figure of merit, defined as the dimensionless quantity

$$\zeta = \frac{\eta^{\text{rel}}}{\sigma L^{\text{rel}}}, \qquad [7]$$

where η^{rel} and L^{rel} are the efficiency and the inductance relatives to the $n = 1$ coil, respectively.

Figure 5D shows the effect of the number of turns on the coil performance as a bar plot of ξ vs n. The initial increase in this figure of merit is due to the fast improvement of the homogeneity with n while the decrease at large n results from the increase of L. A maximum is observed, which indicates that an optimum n exists for a given FOV.

Transverse

To model the G_y gradient coil we used $2n$ straight wires of length $4a$ at $\pm y_i$, $i = 1, \ldots, n$, on each primary plane. In this configuration, the current must flow along x in the same direction in both planes to produce the desired gradient field.

As in the axial case, we calculated the current density, $j_x^d(y)$, in the shielding coil using the analytical relation between the primary and the shielding densities (*12*), which, for $n = 1$, can be written as

$$j_x^d(y) = -\frac{2I}{\pi}\int_0^\infty \cos(y_1\xi)\cos(y\xi)\,\frac{\cosh(a\xi)}{\cosh(d\xi)}\,d\xi. \qquad [8]$$

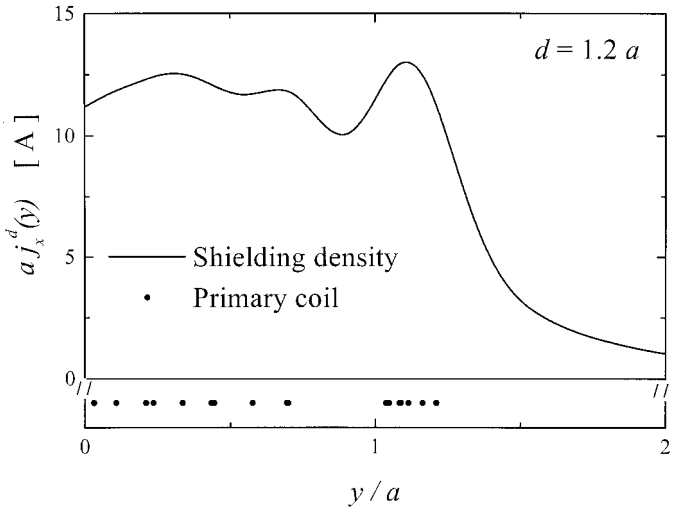

FIG. 6. Primary coil and shielding density for the optimized transverse gradient coil. For this calculation we used $\alpha = 1$, $\beta = 0$, $M = 300$, $S = 50$, $T_{i+1} = T_0(1 - i/S)$, $\Delta y = 0.1\ T_i/T_0$, and $kT_0 = 20$.

To make the current distribution discrete, the positions of the wires in the shielding coil were calculated as in the longitudinal gradient case. As shown in (*12*) the shielding coil can be used as a return path for the primary coil current; therefore no extra wires need to be included in the calculation.

Because of the symmetry of the problem, the y component of the gradient field produced by the k wire has an analytical expression on the $x = 0$ plane, given by

$$G_y^k(y, z) = \frac{\mu_0 Ia}{\pi B^k(y, z)\sqrt{A^k(y, z)}}\left[-(y - y_k)^2 A^k(y, z)^{-1} - 2(y - y_k)^2 B^k(y, z)^{-1} + 1\right], \quad [9]$$

where $A^k(y, z) = (z - z_k)^2 + (y - y_k)^2 + 4a^2$, $B^k(y, z) = (z - z_k)^2 + (y - y_k)^2$, and (y_k, z_k) are the coordinates of the k wire.

As for the longitudinal gradient case we developed a simulated annealing C code including Eqs. [1], [4], [8], and [9] to optimize the transverse gradient coil.

As before the error function evolves to a minimum and the final optimized configurations do not depend on the initial wire arrangement. Figure 6 shows the optimized positions of the 18 wires in the $y > 0$ half primary coil and the shielding coil current density. In the initial arrangement 18 wires were placed at $|y| = 0.4a$ and $d = 1.2a$. The annealing algorithm has been applied, evaluating the gradient field at 100 positions forming a rectangular grid in the plane $(0, y, z)$, for $|y| \le 0.75a$ and $|z| \le 0.75a$.

Figure 7 shows contours maps of the G_y field produced by this coil plotted over a $2a \times 2a$ region. Figure 7A shows the field for the initial wire configuration plotted in the $(0, y, z)$ plane, and Figs. 7B, 7C, and 7D correspond to the optimized wire configuration for the $(0, y, z)$, $(x, 0, z)$, and $(x, y, 0)$ planes, respectively. The efficiency and inductance of this shielded coil for $a = 25$ cm and $d = 1.2a$ are 1.8 mG/cm/A and 315 μH, respectively, where the last was numerically evaluated using (see the Appendix)

$$L = \frac{32a\mu_0}{\pi}\int_0^\infty \Big|\sum_{i=1}^{n}\cos(y_i\xi)\Big|^2 \times\left(1 - \frac{\cosh(a\xi)}{\cosh(d\xi)}e^{-(d-a)\xi}\right)\frac{\cosh(a\xi)}{\xi}e^{-a\xi}d\xi. \quad [10]$$

As for the longitudinal coil set the effect of the number of turns n on the performance of the SA-optimized coil was studied using two different error functions. First we set $\alpha = 1$ and $\beta = 0$, that is, optimizing only homogeneity. Next we set $\alpha = \beta = 0.5$ to equally emphasize the field homogeneity and coil efficiency. In both cases the value of n was varied between 1 and 30 and the results are given in Fig. 8. These results show that the coil efficiency is not an adequate parameter for optimizing the current distribution since it is not very sensitive to the details of this distribution. On the other hand the homogeneity quickly increases with the number of wires, reaching a plateau for $n = 16$. Since the inductance rises quadratically with n an optimum value for the previously defined figure of merit exists as evidenced by the maximum in Fig. 8D.

EXPERIMENTAL

This section describes a gradient set prototype, designed with the proposed method, and the experimental techniques used to test the gradient field linearity and the shielding performance.

The Prototype

Two 5-mm-thick acrylic disks of 28 cm diameter were used to support the longitudinal, G_z, and the transverse, G_x and G_y, gradient coils. The main coils were attached to the disks on their inner sides and the shielding coils on the outer sides. The disks were fixed by an acrylic support in such a way that their interior edges are spaced 7 cm apart from each other as shown schematically in Fig. 9.

Each plane of the longitudinal gradient coil consist of 18 circular wires made of a 0.3-mm-diameter copper rod. The radii of the 18 loops are listed in Table 1, and their layout can be seen in Fig. 10.

This main coil was connected in series with its shielding coil, so that currents flow in the opposite sense. The shielding coil consists of 58 wires made of the same copper rod as the primary coil. The radii of these 58 loops, used to make the shielding current density discrete, are listed in Table 1 and were arranged in four parallel layers. In this way, each coil

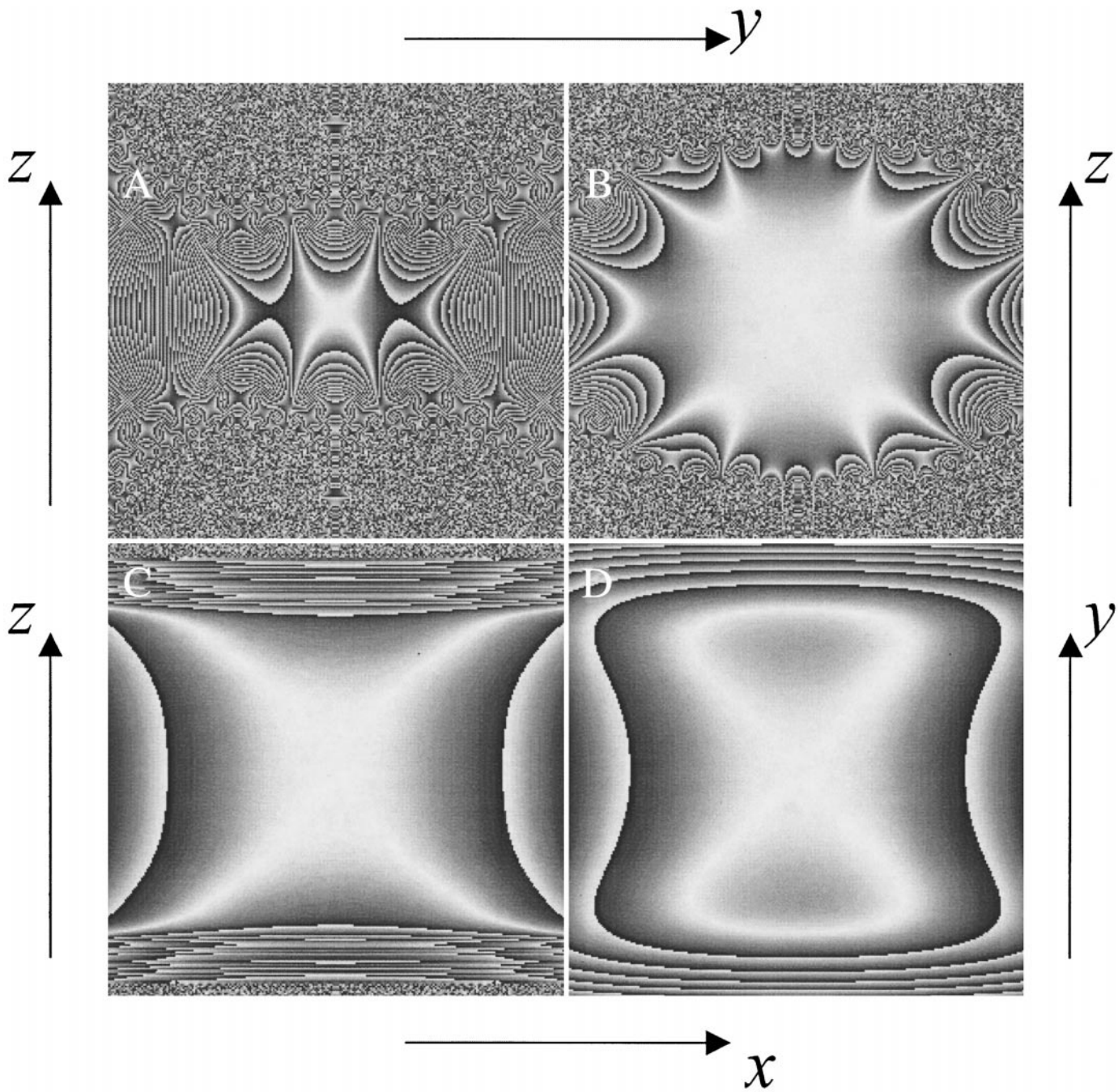

FIG. 7. $2a \times 2a$ maps of the gradient fields due to the transverse gradient coil described in the text. (A) and (B) correspond to (y, z) maps of the initial and optimized configurations, respectively. (C) and (D) are (x, z) and (x, y) maps, respectively, of the field corresponding to the optimized configuration.

forming the shield carries a current $I/4$, improving the matching between the continuous and discrete current densities.

As an example, Fig. 10 shows the coil layout for one of these subcoils. The longitudinal shielding coil was placed directly on the outer side of acrylic disks, resulting in $a/b = 1.14$.

For the self-shielded G_x and G_y gradient coils we used 36 parallel straight copper rods with 20 cm length and 0.5 mm diameter in each primary plane, and 36 parallel copper sheets with 20 cm length, 0.1 mm thickness, and variable width in each shielding plane.

For the return path of each single wire in the primary planes we used a single copper sheet in the shielding planes, fixed to the outer side of the acrylic disks at $z = \pm 4.16$ and ± 4.32 cm for the G_x and the G_y coils, respectively. These coils are similar to rectangular sandwiches formed by two 20×20-cm rectangular solenoids of $(b - a)$ thickness.

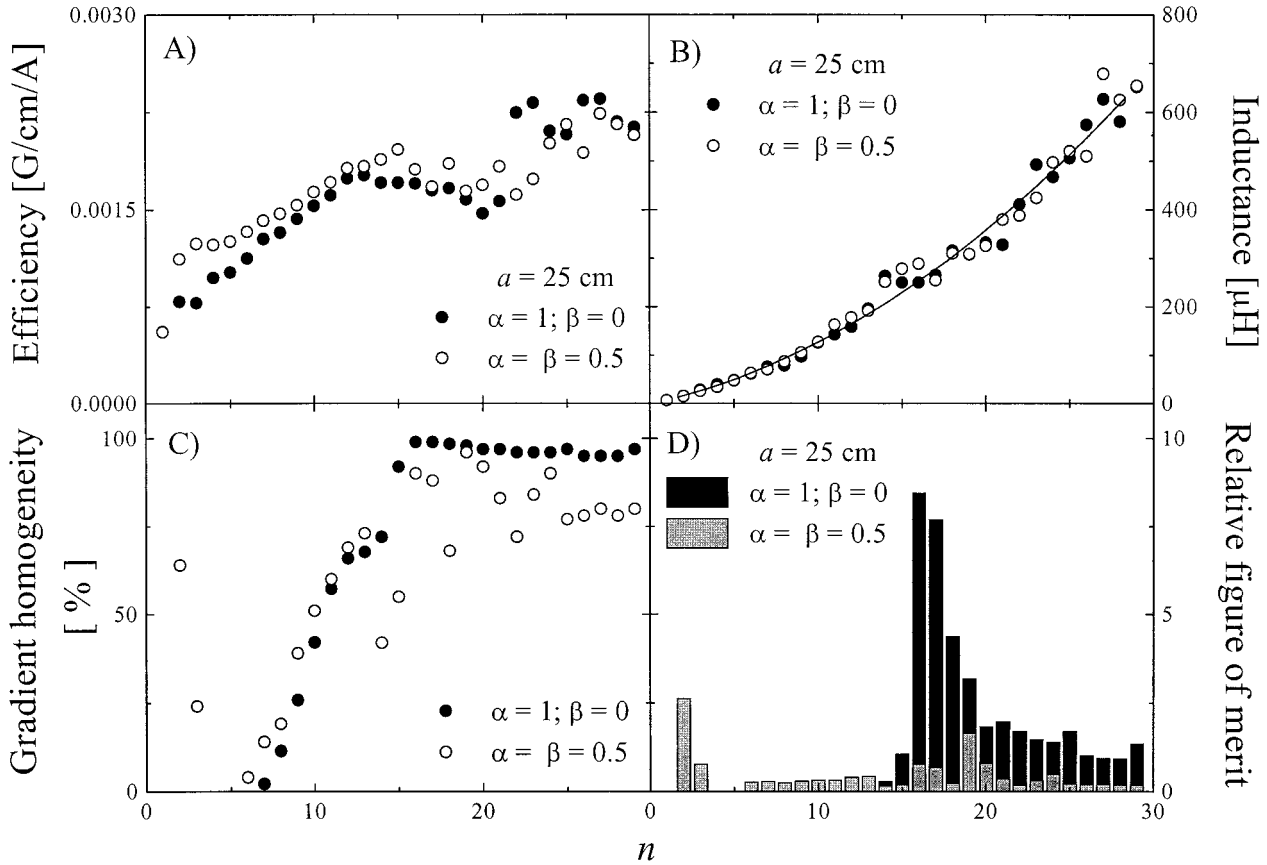

FIG. 8. Main characteristics of the transverse gradient coils as a function of n for $\alpha = 1$; $\beta = 0$, and $\alpha = \beta = 0.5$.

The positions of the copper wires forming the primary plane and the cuts realized on a copper board to build the shielding plane are listed in Tables 2 and 3 for the G_x and G_y coils, respectively. The layout of the primary and shielding G_y coil is illustrated in Fig. 11.

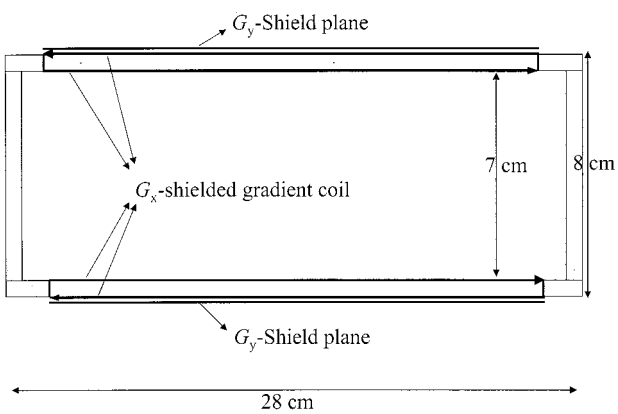

FIG. 9. Schematic drawing of the acrylic support and the direction of currents in both the primary and the shielding G_y coil.

The direction of currents on the primary and the shielding planes for these self-shielded gradient coils is schematically shown in Fig. 9.

For interconnections between the primary and shielding planes we have used a $(b - a)$-length copper rod along z, to avoid the z component of the magnetic field resulting from them.

The measured electric resistance and inductance of the coils are listed in Table 4. The small inductance values, which are proportional to the energy stored in the magnetic field, are due to the small coil gap ($2a = 7$ cm), and are in good agreement with the calculations using [5] and [10] (see Table 4).

Field Linearity

To test the gradient field linearity we used the phase reference method. Recently this method was used to measure the z component of the magnetic fields due to weakly magnetized objects (*20*) and current distributions (*21–23*).

The amplitude images resulting from the phase reference method show the contours of constant magnetic field intensity, avoid the effects of the B_0 field inhomogeneities, and are

TABLE 1
Radii of Circular Wires for the Longitudinal Shielded Gradient Coil (a = 3.5 cm and b/a = 1.143)

Coil	r [cm]					
Main	1.35	2.00	3.75	4.00	4.15	4.40
	4.45	4.55	4.95	5.10	5.15	5.30
	5.65	5.75	6.00	6.10	6.30	
Shield	0.85	1.35	1.60	1.85	2.10	2.35
	2.60	2.85	3.10	3.35	3.65 (2)	3.90 (3)
	4.15 (3)	4.40 (4)	4.65 (4)	4.90 (5)	5.15 (4)	5.40 (4)
	5.65 (4)	5.90 (4)	6.15 (4)	6.40 (3)	6.65 (3)	6.90

Note. Numbers in parentheses indicate the number of loops having the same radius.

TABLE 2
$x \geq 0$ Positions for Straight Wires and Copper Board Cuts of the Transverse G_x Shielded Gradient Coil (a = 3.5 cm and b/a = 1.186)

Coil	x [cm]					
Main	0.00	0.20	0.65	0.80	0.90	1.05
	1.60	1.70 (2)	2.10	2.70	2.85	3.10 (2)
	3.15	3.35	3.40	3.45		
Shield	0.09	0.35	0.61	0.87	1.13	1.39
	1.65	1.92	2.20	2.48	2.75	3.00
	3.25	3.52	3.89	4.38	4.94	5.62

Note. The 18 $\times \leq 0$ positions are symmetric. Numbers in parentheses indicate the number of straight wires having the same position.

calculated from the difference of two gradient recalled echo (GRE) data sets.

To map the magnetic field of the G_x gradient coil we placed a cylindrical phantom with 10 cm diameter and 5 cm length, filled with a 2 mM $CuSO_4$ aqueous solution, inside the gradient set, which was positioned in the isocenter of our full-body Hitachi 0.05-T magnet.

We acquired a transverse image with 10 mm slice thickness and 0.78 mm in-plane resolution. Other experimental parameters were TE = 20 ms, TR = 500 ms, FOV = 20 × 20 cm, 256 × 128 acquisition matrix, and 3.45 mT/m slice selection and 0.75 mT/m readout gradients.

Following the acquisition of this reference data set, we set a DC current of 153 mA in the G_x gradient coil, using a 1.5-V dry cell, and a new amplitude image was acquired with the same protocol as before.

Finally the difference of the two complex data sets was used to obtain the amplitude image shown in Fig. 12a. A similar procedure was used to map the z component of the magnetic field due to the G_y gradient coil. The resulting phase reference image is shown in Fig. 12b. The left part of Fig. 12c is a coronal image of the magnetic field produced by the G_x coil with the same DC current as in Fig. 12a. Finally, the left part of Fig. 12d shows a sagittal image of the magnetic field produced by the G_z coil with a DC current of 81 mA.

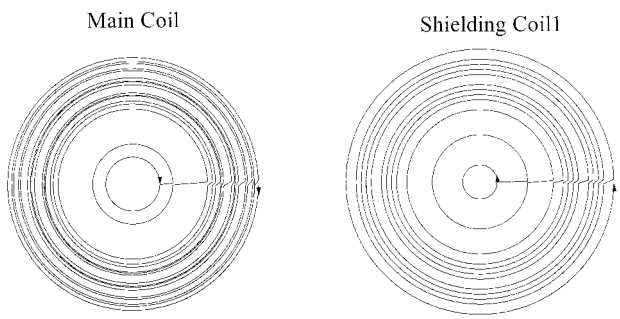

FIG. 10. Schematic drawing of the layout for the G_z coil.

The right parts of Figs. 12c and 12d, showing the magnetic field outside the gradient coils, will be discussed under Shielding Performance.

The black and white strips in the images of Fig. 12 represent contour plots of the magnetic field produced by the gradient coils. The images prove that the gradient field is reasonably linear in a large region inside the coils.

The intensity information of the contour maps can be used to quantify the spatial variation of the magnetic field intensity.

Because of the extra magnetic field, ΔB, due to the current in the gradient coil, the spins at position $\mathbf{r}$ will accumulate an additional phase $\psi = \gamma \Delta B$ TE, which modulates the pixel intensity of the phase reference images (*21*). Since the minimum intensity regions in Fig. 12 correspond to the extra phase, $\psi = 2n\pi$, the difference in field among them is

$$\Delta B = \frac{2\pi}{\gamma \mathrm{TE}} = 11.74 \text{ mG}, \qquad [11]$$

and the local field gradient can be obtained from the spatial distance between the minima.

The linearity of the gradients is shown in Fig. 13, where the z components of the magnetic fields due to the G_x, G_y, and G_z

TABLE 3
$y \geq 0$ Positions for Straight Wires and Copper Board Cuts of the Transverse G_y Shielded Gradient Coil (a = 3.5 cm and b/a = 1.228)

Coil	y [cm]					
Main	0.00	0.25	0.70	0.75	1.10 (2)	1.45
	1.80	1.85	2.40	2.95 (2)	3.05	3.15
	3.20 (2)	3.30	4.80			
Shield	0.06	0.31	0.56	0.81	1.05	1.30
	1.56	1.81	2.06	2.33	2.60	2.84
	3.07	3.29	3.53	3.88	4.43	5.35

Note. The 18 $y \leq 0$ positions are symmetric. Numbers in parentheses indicate the number of straight wires having the same position.

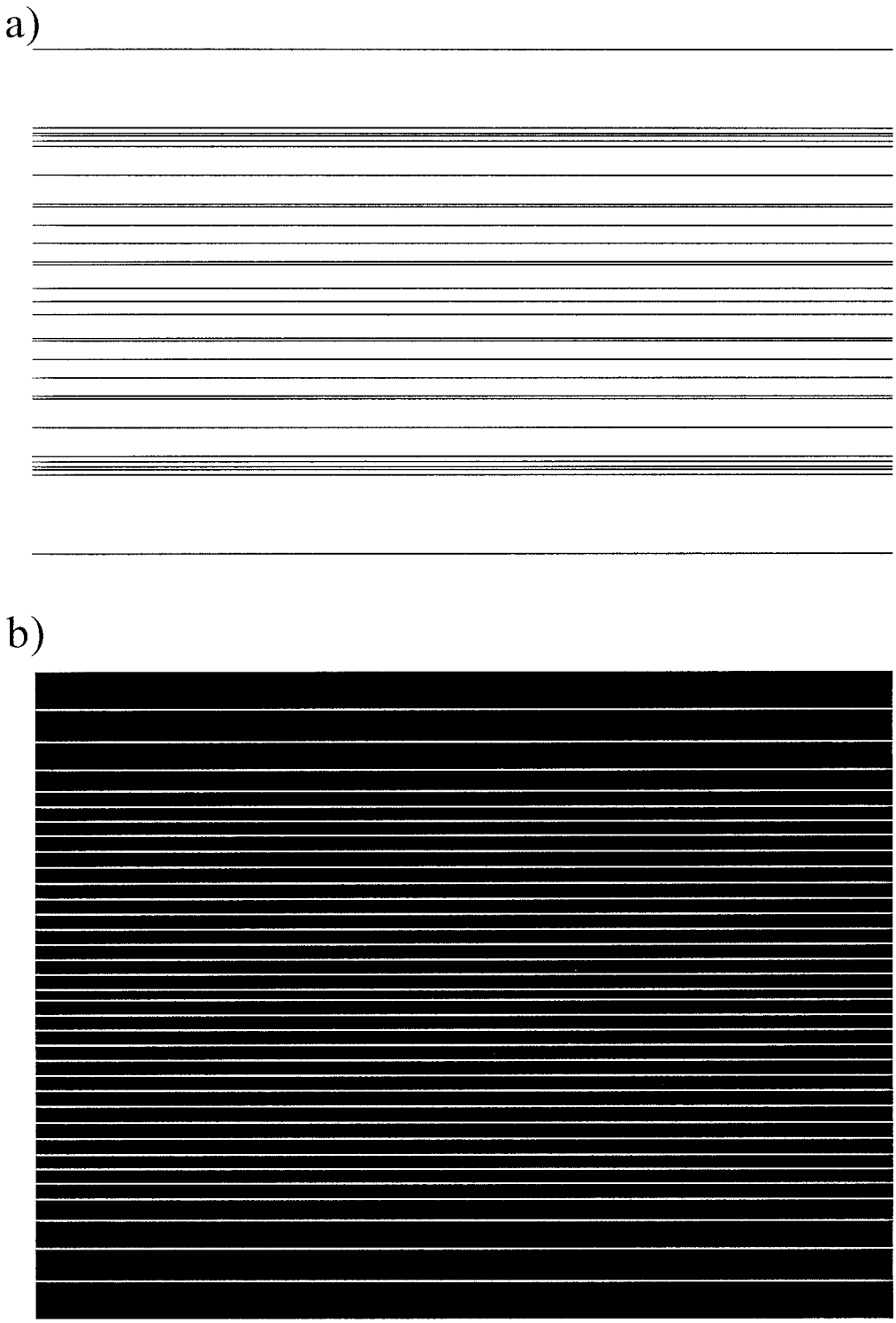

FIG. 11. Schematic drawing of the coil layout for the G_y coil. (a) The layout in the primary plane. (b) The same for the shielding coil.

coils, obtained from Fig. 12 and Eq. [11], are plotted as a function of the distance to the isocenter, along the x, y, and z axis, respectively. The constant slope of all three curves prove the good linearity of the gradient fields. The efficiency of the coils, measured from these magnetic fields, resulted in 1.04 $\pm$ 0.01, 1.10 $\pm$ 0.01, and 1.99 $\pm$ 0.01 mT/m/A for the G_x, G_y,

TABLE 4
Resistance and Inductance of the Gradient Coils

Coil	R [Ω]	L^{exp} [μH]	L^{the} [μH]
G_x	4.4 ± 0.1	68 ± 1	63
G_y	4.4 ± 0.1	56 ± 1	52
G_z	3.0 ± 0.1	28 ± 1	36

and G_z coils, respectively. These values are in good agreement with the corresponding theoretical values 0.86, 0.96, and 2.10 mT/m/A, and the measured limits of the 95% homogeneity regions related to these gradient fields resulted very close to the expected limits.

Shielding Performance

To test the shielding performance, we acquired a set of sagittal images using the phase reference method, placing the phantom described above in the outer region of the gradients, as close as possible to the shielding planes. Magnetic field maps corresponding to the G_x and G_z coils were obtained as before. The maps corresponding to the inner and outer regions, for each gradient, were used to compose Figs. 12c and 12d, which keep the spacing between the regions, to show the shielding performance along both x and z.

From Fig. 12c we can see that the z component of the magnetic field due to the transverse gradient coil is mostly suppressed in the outer region, where it rises to a maximum value of 3.84 μT/A at $z = 5$ cm, representing a suppression of 88% of the z component of the magnetic field at that position. As shown in Fig. 12d, the longitudinal gradient coil presents a similar shielding behavior. For this the maximum value of the magnetic field observed is 5.25 μT/A at position $z = 5$ cm, which represents a suppression of 90% of the z component of the magnetic field. Similar results were found for the G_y gradient coil.

The shielding performance has been examined in a second type of experiment observing the effect of eddy currents on the NMR signal. For these experiments, the gradient set has been placed in a 0.2-T iron magnet with 18-cm-diameter polar pieces and a 10-cm gap. This magnet exhibits poor magnetic field homogeneity due to its small diameter-to-gap ratio. However, the lack of homogeneity did not significantly compromise the examination of eddy current effects. For the interpretation of the eddy current effects it must be noted that the shielding coils of the gradient set were placed directly against the polar pieces of the iron magnet. The direct neighborhood of the shielding coils and the large iron mass of the polar pieces results in a very high sensitivity to eddy current effects.

It must be noticed that the measured inductance of the gradient coil is identical, independently of whether the coils are placed inside or outside the iron magnet. The fact that a large amount of iron mass placed at the exterior of the gradient set and close to the shielding coils does not alter the inductance of the coils gives evidence that the shielding is effective in minimizing the interaction between the pole tips and the gradient coils.

For the acquisition of a NMR signal, we used a solenoid RF coil and a cylindrical phantom with 3 cm diameter and 3 cm length, filled with 2 mM CuSO4 aqueous solution, which were placed 5 mm from the magnet isocenter along z.

We acquired a set of free induction decay (FID) signals under different dynamic situations. For this we switched a gradient pulse with a variable delay before the excitation and acquisition interval. The transients of the gradient pulse induce eddy currents whose effects can be observed in the FID. For the gradient pulse we used a trapezoidal form with 20 ms duration and 100 μs rise time, followed by a delay τ, which was varied in 128 steps from 100 μs to 12.8 ms. Subsequently, we used a nonselective RF excitation pulse and acquired the FID with 256 samples during 16 ms.

In order to observe the eddy current effects we disabled the shielding coils. As shown in Fig. 14a, with the G_z shielding disabled and for short delay values, $\tau = 500$ μs, the gradient transient produces a time-dependent magnetic field gradient, which produces a modulation of the FID. No modulation of the FID due to eddy current effects is observed for sufficiently long delay values, $\tau = 12.5$ ms, as shown in Fig. 14b. Finally, Fig. 14c shows that with shielding enabled, even for short delays, $\tau = 500$ μs, no modulation is observed. This proves the efficiency of the gradient shield in minimizing eddy currents induced in the pole tips.

The one-dimensional fast Fourier transforms of the FIDs in Figs. 14a to 14c, plotted in Fig. 14d, show the overall behavior in the frequency domain. When the shielding is off, the frequency distribution corresponding to the $\tau = 500$ μs transformed data exhibits several peaks as a result of the spread in Larmor frequency induced by a time-dependent magnetic field gradient due to the eddy currents. For the $\tau = 12.5$ ms transformed data a single peak is observed, showing less eddy current effects at that delay time. As is also shown in this figure, when the shielding is turned on, the Larmor frequency spread is mostly avoided because of the magnetic field nulling at the pole tips positions.

Imaging Test

To show the quality of the gradient fields in producing NMR images we placed the biplanar gradient set at the isocenter of the 0.05-T Hitachi magnet, coaxially with B_0.

We set the NMR probe, tuned at 2.35 MHz, and the cylindrical phantom, described above, at the gradient isocenter and acquired a set of SE 256 × 128 images by using a 10 cm × 10 cm FOV, TR = 500 ms, and TE = 20 ms, without selection gradient.

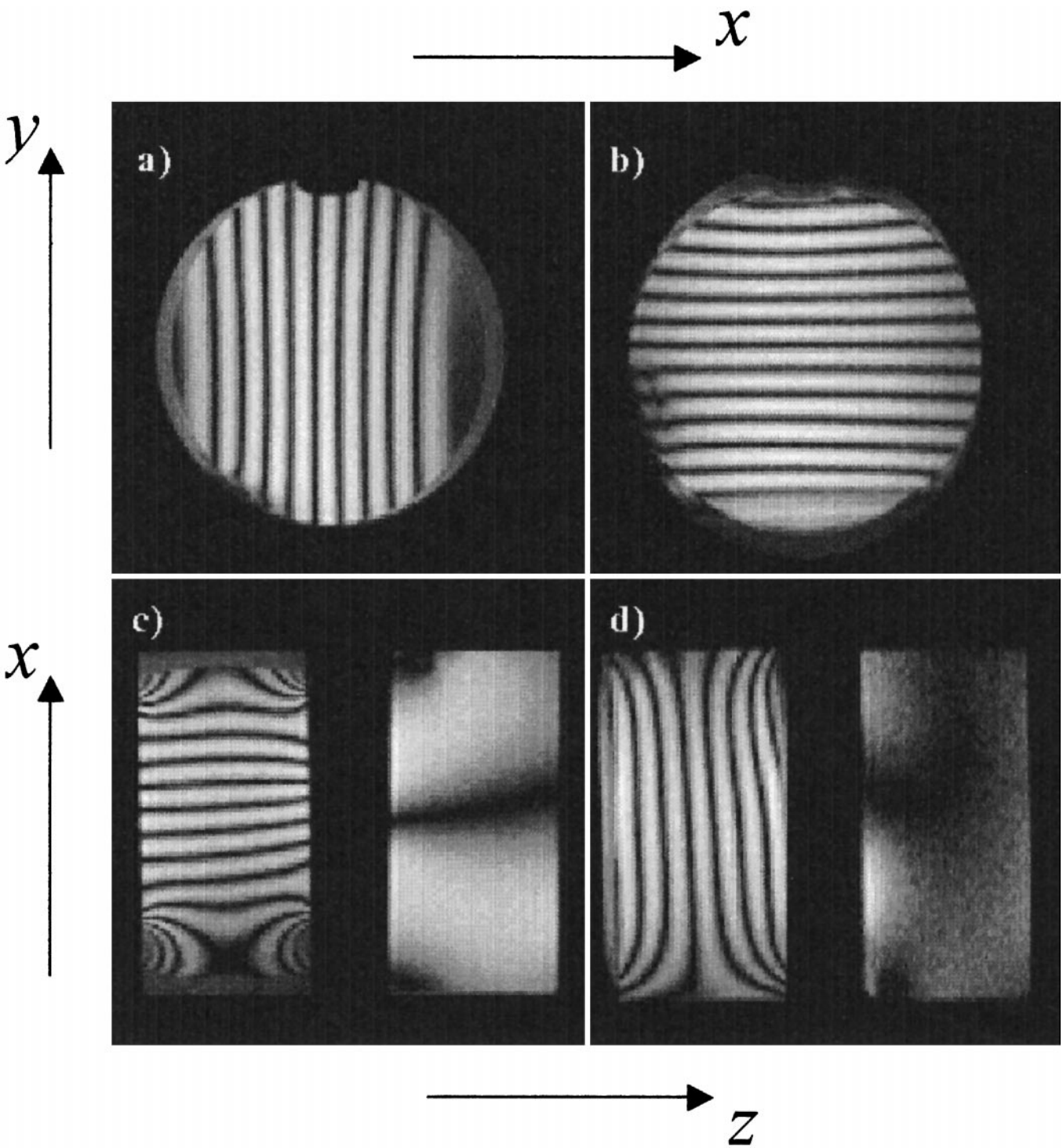

FIG. 12. Phase reference images showing the contours of the constant B_z field. The (a) and (b) transverse images correspond to the G_x and the G_y coils, and the coronal images (c) and (d) correspond to the G_x and G_z coils, respectively.

The coronal and sagittal planar projection images acquired are shown in Fig. 15. As we can see, the phantom edges did not suffer distortions from gradient nonlinearity even at a large FOV in the z direction of about half the gap size.

SUMMARY

The SA method can greatly improve the design of high-performance gradient coils. When the standard SA algorithm

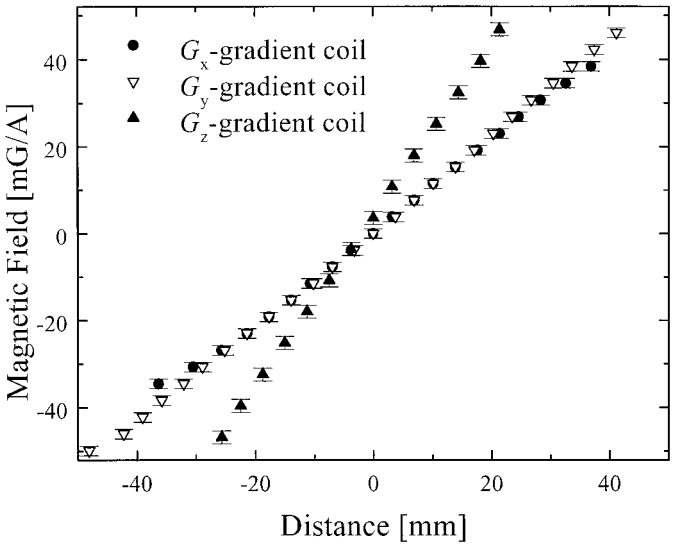

FIG. 13. Magnetic field as a function of the distance from the gradient isocenter along the *x*, *y*, and *z* axis for the G_x, G_y, and G_z coils, respectively.

(*15*) is applied to the optimization of self-shielded coils, the increase in the necessary number of degrees of freedom results in long computing times. As shown in this paper, the proposed modified SA procedure, which uses the analytical relationship between primary and shielding currents, allows a great reduction in the number of degrees of freedom.

The computing time can be further reduced by restricting the wire geometries to those that allow analytical calculation of the magnetic field over selected regions that can then be used to evaluate the error function used in the annealing procedure.

The examples presented in this paper show that this description does not impoverish the quality of the result.

The present approach resulted in approximately 30 min of computing time even using a double-precision nonoptimized C code running on a standard 166-MHz Pentium PC under DOS.

Additionally we have derived generic expressions for the inductance of shielded biplanar gradient coils, which were applied to calculate the coil inductance and used to show that an optimum number of wires exists for this geometry.

Finally, we did a prototype of the shielded biplanar gradient set to test the proposed design method. The inductance, effi-

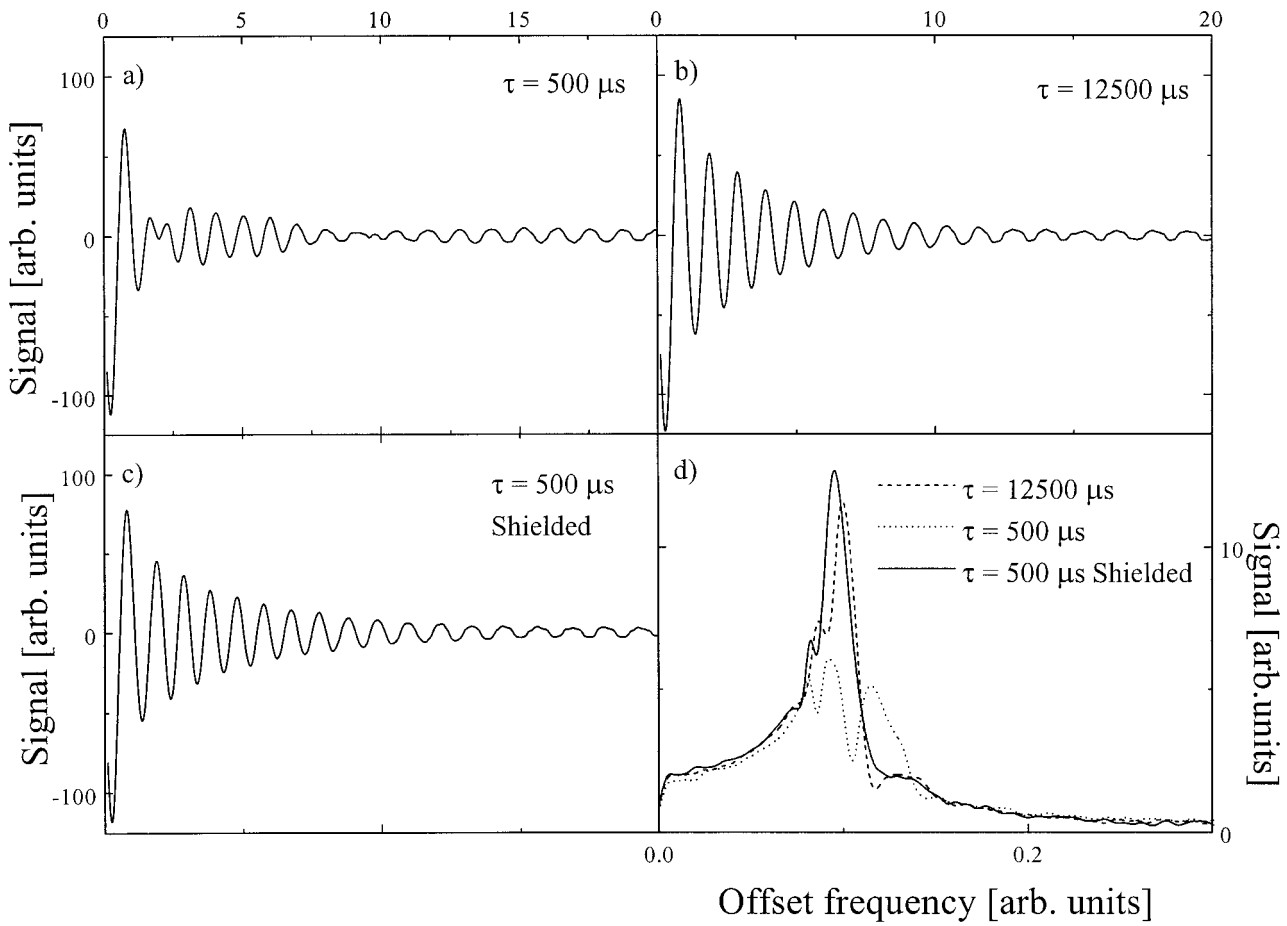

FIG. 14. FID signals relating magnetization evolution, after a trapezoidal G_z gradient pulse, with the eddy current induced on the polar tips of a 0.2-T 10-cm-gap iron magnet. Slew rate = 140 T/m/s.

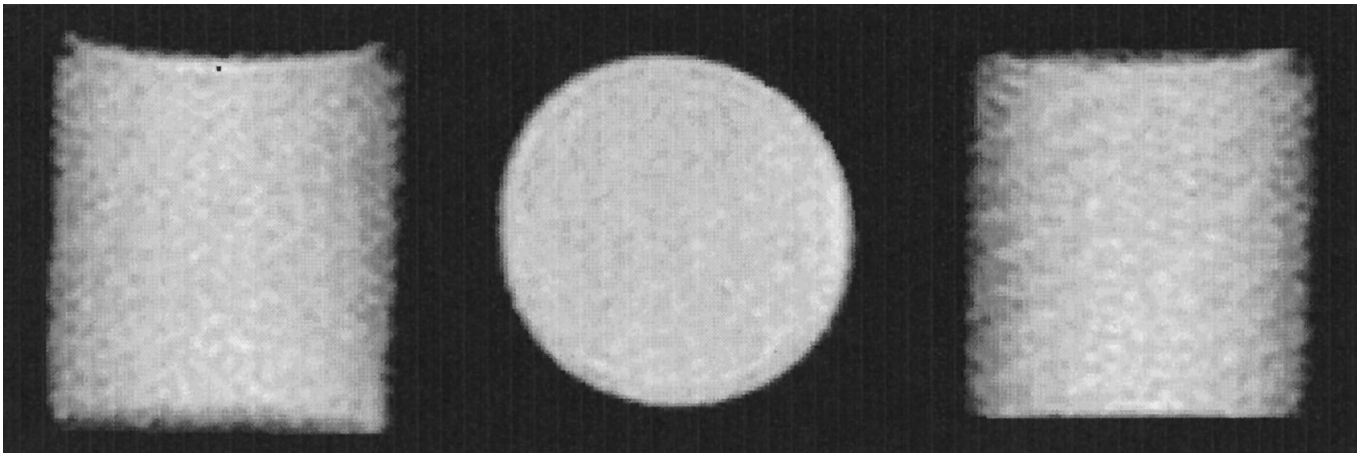

FIG. 15. MR planar projections of a 3-cm-diameter cylindrical phantom, for which the biplanar gradient coil was used for the phase and frequency encoding. $B_0 = 0.05$ T.

ciency, linearity, and shielding performance of gradient coils are in good agreement with theoretical expectations.

APPENDIX

In this Appendix we derive the analytical expression of the inductance for the longitudinal and transverse gradient coils.

The inductance of a system of two coils connected in series can be written as

$$L = L_{11} + L_{22} + L_{21} + L_{12}, \qquad [12]$$

where the induction coefficients, L_{ij}, are defined by (*19*)

$$L_{ij} = \frac{1}{I_i I_j} \int_V \mathbf{J}_i \cdot \mathbf{A}_j dV, \qquad [13]$$

$\mathbf{J}_i$ being the current density of the i coil and $\mathbf{A}_j$ the vector potential of the j coil.

Using the three-dimensional Fourier expansion of the vector potential $\mathbf{A}$, as given in Ref. (*10*), the Fourier transform of the (x, y) component of the current density (*12*), $j_{xy}(k_x, k_y)$, and the continuity equation expressed in terms of the Fourier components of the current density (*12*), we have found the following expression for the inductance of a shielded biplanar gradient coil,

$$\begin{aligned} L = \frac{\mu_0}{8\pi^2 I^2} \int_{-\infty}^{\infty}\int_{-\infty}^{\infty} \{ & |j_x^a(k_x, k_y)|^2 + |j_x^{-a}(k_x, k_y)|^2 \\ & + 2e^{-2a\sqrt{k_x^2+k_y^2}} j_x^{a*}(k_x, k_y) j_x^{-a}(k_x, k_y) \\ & + |j_x^d(k_x, k_y)|^2 + |j_x^{-d}(k_x, k_y)|^2 \\ & + 2e^{-2d\sqrt{k_x^2+k_y^2}} j_x^{d*}(k_x, k_y) j_x^{-d}(k_x, k_y) \\ & + 2[e^{-(d-a)\sqrt{k_x^2+k_y^2}} (j_x^{a*}(k_x, k_y) j_x^d(k_x, k_y) \\ & + j_x^{-a*}(k_x, k_y) j_x^{-d}(k_x, k_y)) \\ & + e^{-(d+a)\sqrt{k_x^2+k_y^2}} (j_x^{a*}(k_x, k_y) j_x^{-d}(k_x^2 + k_y^2) \\ & + j_x^{-a*}(k_x, k_y) j_x^d(k_x, k_y))]\} \frac{\sqrt{k_x^2 + k_y^2}}{k_y^2} dk_x dk_y, \end{aligned} \qquad [14]$$

where $\mathbf{k} = (k_x, k_y, k_z)$ is a vector in the reciprocal space. Considering now the symmetric ($\mathbf{j}(x, y, z) = \mathbf{j}(x, y, -z)$) and antisymmetric ($\mathbf{j}(x, y, z) = -\mathbf{j}(x, y, -z)$) current distributions and the shielding condition for each case (*12*)

$$j_x^d(k_x, k_y) = -j_x^a(k_x, k_y) \frac{f_a(k_x, k_y)}{f_d(k_x, k_y)}, \qquad [15]$$

with $f_\alpha(k_x, k_y) = \sinh(\alpha\sqrt{k_x^2+k_y^2})$ for the antisymmetric case and $f_\alpha(k_x, k_y) = \cosh(\alpha\sqrt{k_x^2 + k_y^2})$ for the symmetric case, Eq. [14] can be simplified to

$$\begin{aligned} L = \frac{\mu_0}{2\pi^2 I^2} \int_{-\infty}^{\infty}\int_{-\infty}^{\infty} & |j_x^a(k_x, k_y)|^2 \\ & \times \left(1 - e^{-(d-a)\sqrt{k_x^2+k_y^2}} \frac{f_a(k_x, k_y)}{f_d(k_x, k_y)}\right) \\ & \times \frac{\sqrt{k_x^2 + k_y^2}}{k_y^2} f_a(k_x, k_y) e^{-a\sqrt{k_x^2+k_y^2}} dk_x dk_y. \end{aligned} \qquad [16]$$

For the axial gradient coil we have an antisymmetric configuration consisting of n loops on each gradient coil plane, $z = \pm a$, with the primary current I. Thus, for this geometry, the current distribution at the Fourier space is given by

$$j_x^a(k_x, k_y) = 2\pi I \frac{k_y}{q} \sum_{i=1}^{n} R_i J_1(R_i q), \qquad [17]$$

where $q = \sqrt{k_x^2 + k_y^2}$. Therefore the inductance for this gradient coil is

$$L = 4\pi\mu_0 \int_0^\infty \Big|\sum_{i=1}^{N} R_i J_1(R_i q)\Big|^2 \times \left(1 - \frac{\sinh(aq)}{\sinh(dq)}\, e^{-(d-a)q}\right) \sinh(aq) e^{-aq} dq. \quad [18]$$

For the transverse gradient coil we have considered n straight wires parallel to the x axis, symmetrically distributed respect to the $y = 0$ axis, on each of the planes at $z = \pm a$ and symmetrically distributed with respect to the $y = 0$ axis with length l. The x component of this symmetric current density at the Fourier space can be written as

$$j_x^a(k_x, k_y) = 4\pi I \frac{\sin(k_x l/2)}{k_x} \sum_{i=1}^{N} \cos(k_y y_i). \quad [19]$$

Hence for the inductance we have

$$L = 8\mu_0 \int_{-\infty}^{\infty}\int_{-\infty}^{\infty} \left|\frac{\sin(k_x l/2)}{k_x} \sum_{i=1}^{N} \cos(k_y y_i)\right|^2 \times \left(1 - e^{-(d-a)\sqrt{k_x^2+k_y^2}} \frac{\cosh(a\sqrt{k_x^2 + k_y^2})}{\cosh(d\sqrt{k_x^2 + k_y^2})}\right) \times \frac{\sqrt{k_x^2 + k_y^2}}{k_y^2} \cosh(a\sqrt{k_x^2 + k_y^2}) e^{-a\sqrt{k_x^2+k_y^2}} dk_x dk_y, \quad [20]$$

which for $l \gg a$ can be written as

$$L = \frac{8\mu_0 l}{\pi} \int_0^\infty \Big|\sum_{i=1}^{n} \cos(k_y y_i)\Big|^2 \times \left(1 - \frac{\cosh(ak_y)}{\cosh(dk_y)}\, e^{-(d-a)k_y}\right) \frac{\cosh(ak_y)}{k_y}\, e^{-ak_y} dk_y. \quad [21]$$

ACKNOWLEDGMENTS

We acknowledge Professor Alberto Tannús for his fruitful comments about techniques for measuring the effects of eddy currents on FID signals. We also acknowledge financial support from CLAF, FINEP/PADCT, and CNPq. This research was also supported by FAPESP Project 96/05437-0.

REFERENCES

1. R. Turner, Gradient coil design: A review of methods, *Magn. Reson. Imaging* **11,** 903–920 (1993).
2. J. M. Jin, "Electromagnetic Analysis and Design in Magnetic Resonance Imaging," CRC Press, Boca Raton, FL (1998).
3. R. Turner, A target field approach to optimal coil design, *J. Phys. D: Appl. Phys.* **19,** L147–L151 (1986).
4. R. Turner and R. M. Bowley, Passive screening of switched magnetic field gradients, *J. Phys. E: Sci. Instrum.* **19,** 876–879 (1986).
5. R. Turner, Minimum inductance coils, *J. Phys. E: Sci. Instrum.* **21,** 948–952 (1988).
6. J. W. Carlson, K. A. Derby, K. C. Hawryszko, and M. Weideman, Design and evaluation of shielded gradient coils, *Magn. Reson. Med.* **26,** 191–206 (1992).
7. B. A. Chronik and B. K. Rutt, Constrained length minimum inductance gradient coil design, *Magn. Reson. Med.* **39,** 270–278 (1998).
8. K. Yoda, Analytical design method of self-shielded planar coils, *J. Appl. Phys.* **67,** 4349–4353 (1990).
9. R. Bowtell and P. Mansfield, Minimum power, flat gradient pairs for NMR microscopy, 8th ISMRM (1990).
10. M. A. Martens, L. S. Petropoulos, R. W. Brown, and J. H. Andrews, Insertable biplanar gradient coils for magnetic resonance imaging, *Rev. Sci. Instrum.* **62,** 2639–2645 (1991).
11. S. Y. Lee, B. S. Park, H. Y. Jeong, and W. Yi, Planar gradient coil design by scaling the spatial frequencies of minimum-inductance current density, *Magn. Reson. Med.* **38,** 858–861 (1997).
12. E. C. Caparelli, D. Tomasi, and H. Panepucci, Shielded biplanar gradient coil design, *J. Magn. Reson. Imaging* **9,** 725–731, (1999).
13. S. Crozier and D. M. Doddrell, Gradient-coil design by simulated annealing, *J. Magn. Reson. A* **103,** 354–357 (1993).
14. S. Crozier, L. K. Forbes, and D. M. Doddrell, The design of transverse gradient coils of restricted length by simulated annealing, *J. Magn. Reson. A* **107,** 126–128 (1994).
15. S. Crozier and D. M. Doddrell, A design methodology for short, whole-body, shielded gradient coils for MRI, *Magn. Reson. Imaging* **13,** 615–620 (1995).
16. M. L. Buszko, M. F. Kempka, E. Szczesniak, D. C. Wang, and E. R. Andrew, Optimization of transverse gradient coils with coaxial return paths by simulated annealing, *J. Magn. Reson. B* **112,** 207–213 (1996).
17. A. M. Peters and R. W. Bowtell, Biplanar gradient coil design by simulated annealing, *Magn. Reson. Mater. Phys. Biol. Med.* **2,** 387–389 (1994).
18. N. Metropolis, A. W. Rosenbluth, M. N. Rosenbluth, and A. H. Teller, Equation of state calculations by fast computing machines, *J. Chem. Phys.* **21,** 1087–1092 (1953).
19. R. Feynman, R. B. Leighton, and M. Sands, "The Feynman Lectures on Physics, Mainly Electromagnetism and Matter," Vol. II, Addison–Wesley, Reading, MA (1964).
20. D. Tomasi, H. Panepucci, E. L. Vidoto, and E. Ribeiro Azevedo, Use of a phase reference for field mapping with amplitude images at low field, *J. Magn. Reson.* **131,** 310–314 (1998).
21. D. Tomasi and H. Panepucci, Magnetic fields mapping with the phase reference method, *Magn. Reson. Imaging* **17,** 157–160 (1998).
22. D. Tomasi and H. Panepucci, Magnetic fields mapping with the phase reference method, Sixth Scientific Meeting and Exhibition of the ISMRM, Sydney, Australia (1998).
23. D. Tomasi, H. Panepucci, E. L. Vidoto, M. R. Zucchi, and E. Ribeiro Azevedo, Mapping the magnetic fields of current distributions, 29th AMPERE–13th ISMAR International Conference on Magnetic Resonance & Related Phenomena, Berlin, Germany (1998).